Nanoscale

van der Waals Epitaxy of Highly (111)-Oriented BaTiO3 on MXene

Journal:	*Nanoscale*
Manuscript ID	NR-ART-09-2018-007140.R1
Article Type:	Paper
Date Submitted by the Author:	13-Nov-2018
Complete List of Authors:	Bennett-Jackson, Andrew; Drexel University, Materials Science and Engineering Falmbigl, Matthias; Institute of Physical Chemistry, University of Vienna Hantanasirisakul, Kanit; Drexel University College of Engineering, Materials Science and Engineering; A. J. Drexel Nanomaterials Institute, Gu, Zongquang; Drexel University, Materials Science + Engineering Imbrenda, Dominic; Drexel University, Electrical & Computer Engineering Plokhikh, Aleksandr; Drexel University, Materials Science + Engineering Will-Cole, Alexandria; Drexel University, Materials Science and Engineering Hatter, Christine; Drexel University, Materials Science and Engineering Wu, Liyan; University of Pennsylvania Anasori, Babak; Drexel University, Materials Science and Engineering Gogotsi, Yury; Drexel University, Materials Science and Engineering Spanier, Jonathan; Drexel University, Materials Science + Engineering

Journal Name

ARTICLE

van der Waals Epitaxy of Highly (111)-Oriented $BaTiO_3$ on MXene

Andrew L. Bennett-Jackson,[a] Matthias Falmbigl,[a] Kanit Hantanasirisakul,[a,b] Zongquan Gu[a,c], Dominic Imbrenda,[a,c] Aleksandr V. Plokhikh,[a] Alexandria Will-Cole,[a] Christine Hatter,[a,b], Liyan Wu,[d] Babak Anasori,[a,b] Yury Gogotsi,[a,b] and Jonathan E. Spanier*[a,c,e]

Received 00th January 20xx,
Accepted 00th January 20xx

DOI: 10.1039/x0xx00000x

www.rsc.org/

We report on the high temperature thin film growth of $BaTiO_3$ on $Ti_3C_2T_x$ MXene flakes using van der Waals epitaxy on a degradable template layer. MXene was deposited on amorphous and crystalline substrates by spray- and dip-coating techniques, while the growth of $BaTiO_3$ at 700 °C was accomplished using pulsed laser deposition in an oxygen rich environment. We demonstrate that the MXene flakes act as a temporary seed layer, which promotes highly oriented $BaTiO_3$ growth along the (111) direction independent of the underlying substrate. The lattice parameters of the $BaTiO_3$ films are close to the bulk value suggesting that the $BaTiO_3$ films remains unstrained, as expected for van der Waals epitaxy. The initial size of the MXene flakes has an impact on the orientation of the $BaTiO_3$ films with larger flake sizes promoting a higher fraction of the polycrystalline film to grow along the (111) direction. The deposited $BaTiO_3$ film adopts the same morphology as the original flakes and piezoresponse force microscopy shows a robust ferroelectric behavior for individual grains. Transmission electron microscopy results indicate that the $Ti_3C_2T_x$ MXene fully decomposes during the $BaTiO_3$ deposition and the surplus Ti atoms are readily incorporated into the $BaTiO_3$ film. Electrical measurements show a similar dielectric constant as a $BaTiO_3$ film grown without the MXene seed layer. The demonstrated process has the potential to overcome the longstanding issue of integrating highly oriented complex oxide thin films directly on any desired substrate.

Introduction

Perovskite oxide thin films offer a wide range of physical properties[1] including ferroelectricity for highly tunable and low-loss dielectric permittivity,[2] for high photogenerated carrier mobility in a band insulator,[3] for tip-enhanced intrinsic photovoltaic response,[4] and for large piezoelectricity and pyroelectricity,[5] and ferromagnetism,[6] multiferroicity,[7,8] and superconductivity.[9] Thin films of these perovskite oxides allow for controlled manipulation of nanoscale phenomena, such as domain walls, which can enhance polarization and other physical properties.[10–12] Heteroepitaxial growth of thin film perovskite oxides can provide opportunities to tune these physical properties, but is greatly reliant on the chosen substrate.[13-17] Recently, orders of magnitude enhancement in dielectric constant has been realized in $PbZr_{0.2}Ti_{0.8}O_3$ ferroelectric thin films grown on (111) $SrTiO_3$ (STO) substrates. The high symmetry in (111) orientation leads to a manifold of polarization directions and hence complex nanotwinned ferroelectric domain structure. The high domain wall density spurs the extrinsic contribution in the dielectric properties and provides alternate switching paths on the potential landscape, saving more energy than 180° reversal switching.[16]

While in recent years the availability of single-crystalline perovskite oxide substrates has allowed for such control of thin films, the lattice mismatch between the film and substrate must be small for strain-coherent and dislocation-free films produced by high temperature deposition techniques such as pulsed laser deposition (PLD) and molecular beam epitaxy (MBE). However, the substrate choice for the film growth is limited by cost and on-wafer integration. Additionally, the use of MBE and hybrid metal organic chemical vapor deposition-MBE has grown high quality STO[18,19] and BTO[20,21] on Si (001), however several processing steps are required to first remove the native SiO_2 and then grow the oxide film without oxidizing the Si/oxide interface. Thus, it would be highly beneficial to utilize ubiquitous substrates such as glass, silicon, or sapphire for easier integration into current microelectronics as well as the capability to transfer these functional thin films onto flexible substrates after the deposition with minimal processing steps.

The use of van der Waals epitaxy,[22,23] which was applied by Koma *et al.* in the 1990's, is an approach to grow 3D semiconductor thin film materials on 2D layered materials substrates with a large lattice mismatch.[24] This process uses thin 2D sheets of layered material, which acts as a seed layer to

[a] *Department of Materials Science & Engineering, Drexel University, Philadelphia, PA 19104, USA*
[b] *A.J. Drexel Nanomaterials Institute, Drexel University, Philadelphia, PA 19104, USA*
[c] *Department of Electrical & Computer & Engineering, Drexel University, Philadelphia, PA 19104, USA*
[d] *Department of Materials Science & Engineering, University of Pennsylvania, Philadelphia, PA 19104, USA*
[e] *Department of Physics, Drexel University, Philadelphia, PA 19104, USA*
* *email: spanier@drexel.edu*
†*Electronic Supplementary Information (ESI) available: See*
DOI: 10.1039/x0xx00000x

promote crystalline and oriented growth of the thin film overlayers. The bonds between the 2D layer and the thin film are of van der Waals character and therefore significantly weaker than the ionic and/or covalent bonds typically formed between the film and single-crystalline substrates.[25] Hence, a larger difference in the lattice mismatch and the thermal expansion coefficient can be accommodated without the formation of dislocations at the thin film-substrate interface. Recent works have used nanosheets of $Ca_2Nb_3O_{10}$,[26-28] MoO_2,[29] and graphene[22,30] as seed layers to promote oriented thin film growth on various substrates. While these methods have proven that oriented crystalline growth is attainable on ubiquitous substrates, one downside of this approach is that the nanosheet seed layer with its properties inherently becomes a part of the thin film heterostructure,[31] which is not always desirable, limiting its applicability.

In order to remove this constraint, it would be essential to have a decomposable seed layer, which can promote oriented crystalline growth on various substrates without affecting the functionality of the thin film overlayer. In this paper, we report on the utilization of the 2D titanium carbide $Ti_3C_2T_x$ (MXene)[32] as a decomposable seed layer, which does not require additional processing steps to remove it from the resulting thin film. $BaTiO_3$ (BTO) grown by PLD was selected since BTO is a well-characterized archetypical ferroelectric oxide perovskite material.[33] Among a variety of MXenes available to date,[34] oxygen terminated $Ti_3C_2T_x$ is chosen as a seed layer for the BTO growth because of its titanium-based chemistry compatible with $BaTiO_3$. Both materials are well studied in their respective classes (2D transition metal carbides and ferroelectric oxide perovskite). Given that most (if not all) MXenes have the same hexagonal structure, they should act as a degradable seed layer for BTO thin film growth. The MXene can be produced in large quantities with controlled size of single-layer 2D flake, and it can be coated on various substrates from solution.[35] Moreover, we demonstrated that the Ti atoms of the MXene layer are incorporated into the BTO structure during the growth process. The energy dispersive spectroscopy line scan, shows only a slight increase in Ti concentration from the bottom to the top electrode. We therefore believe that the common chemistry is not necessary for the templating effect observed.

BTO thin films were deposited by PLD onto fused silica and (111) Pt/Si substrates with a thin (≈12 or ≈64 nm thick, Supporting Information) MXene film on top. Results reveal a strong templating effect of MXene yielding highly oriented growth of BTO films along the (111) direction, suggesting that the degree of orientation can be controlled by the initial flake size of the MXene film. Atomic force microscopy images reveal a similarity of the PLD-grown BTO film grain size and shape to the typical initial MXene flakes (Fig. 3(a), (b), and S4 - S6)), whereas cross-section transmission electron microscopy indicates a negligible amount of amorphous material and defects at the interface between Pt and BTO thin film. Switching spectroscopy piezoresponse force microscopy (SS-PFM) gives the iconic "butterfly" loop demonstrating evidence of switching of local film plane-normal ferroelectric polarization in the BTO film grown on the MXene seed layer.

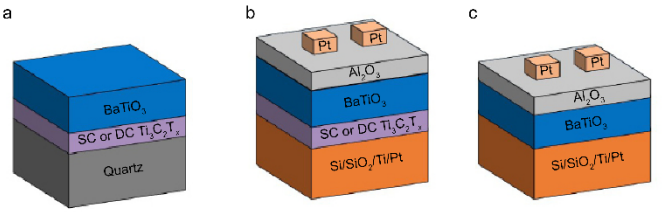

Fig. 1 Schematics showcasing the different film stacks. The structure in (a) was utilized twice with either the spray-coating (SC) or dip-coating (DC) method with a thickness of 12 nm or 64 nm of $Ti_3C_2T_x$ MXene, followed by 100 nm of $BaTiO_3$ (BTO). (b) 12 nm of the MXene deposited by SC on a Pt-silicon wafer, followed by 100 nm of BTO, then 3 nm of Al_2O_3, and finally 90 nm of Pt for the top electrodes. (c) 100 nm of BTO was deposited on a Pt-silicon wafer, followed by 3 nm of Al_2O_3, and finally 120 nm of Pt for the top electrodes.

Experimental

The MXene films were synthesized following the procedure described in the Supporting Information and deposited (Fig. S1, 2) on the surface of quartz substrates and commercially available Pt (111)/Ti/SiO_2/Si (001) wafers (Pt-silicon). Two methods, spray-coating and dip-coating, were used to deposit the MXene solution onto the substrates following procedures described elsewhere.[35] The average lateral size of MXene flakes utilized for the spray-coating method was about 5 µm, while for the dip-coating method the average flake size was about 1 µm. A set of various thin film stacks were synthesized to examine the effects of the MXene layers on the BTO film. For the deposition sequence outlined in Fig. 1(a), spray-coated MXene layers with thicknesses of about 12 nm or 64 nm were utilized (Fig. S4 - S6). In both cases, BTO was deposited onto the quartz/MXene heterostructure by PLD. For another set of samples, shown in Fig 1(b), MXene was spray coated on the surface of (111) Pt-silicon (after treating the surface with Piranha acid solution to make it hydrophilic) followed by a subsequent growth of BTO by PLD. For comparison, a BTO thin film of the same thickness was directly grown on a Pt-silicon substrate without the MXene seed layer under the same conditions. Onto each of these films (Fig. 1(b) and (c)) a layer of 3 nm thick of Al_2O_3 was deposited by atomic layer deposition (ALD) in a separate step followed by sputtering of platinum top electrodes to produce metal-insulator-metal (MIM) capacitors.

Results and Discussion

X-ray Diffraction

The X-ray diffraction (XRD) scan of the MXene on quartz reveals a peak at ≈7°, corresponding to the (002) Bragg-peak of the MXene layers, which yields a *c*-lattice parameter of 22 Å, indicating the presence of residual water between the $Ti_3C_2T_x$ layers.[34] In addition, a broad peak located at ≈21.5° (red spectrum in Fig. 2(a)) corresponding to the amorphous quartz substrate, is apparent in the XRD scans (Fig. 2(a)). After the high temperature BTO deposition the low angle peak vanishes, suggesting that the MXene layer decomposed during the BTO deposition resulting from the low stability of $Ti_3C_2T_x$ in air at high temperatures.[34] However, comparing the XRD pattern for the BTO growth on quartz with and without the MXene layer (blue and brown traces in Fig 2(a), respectively), two key results

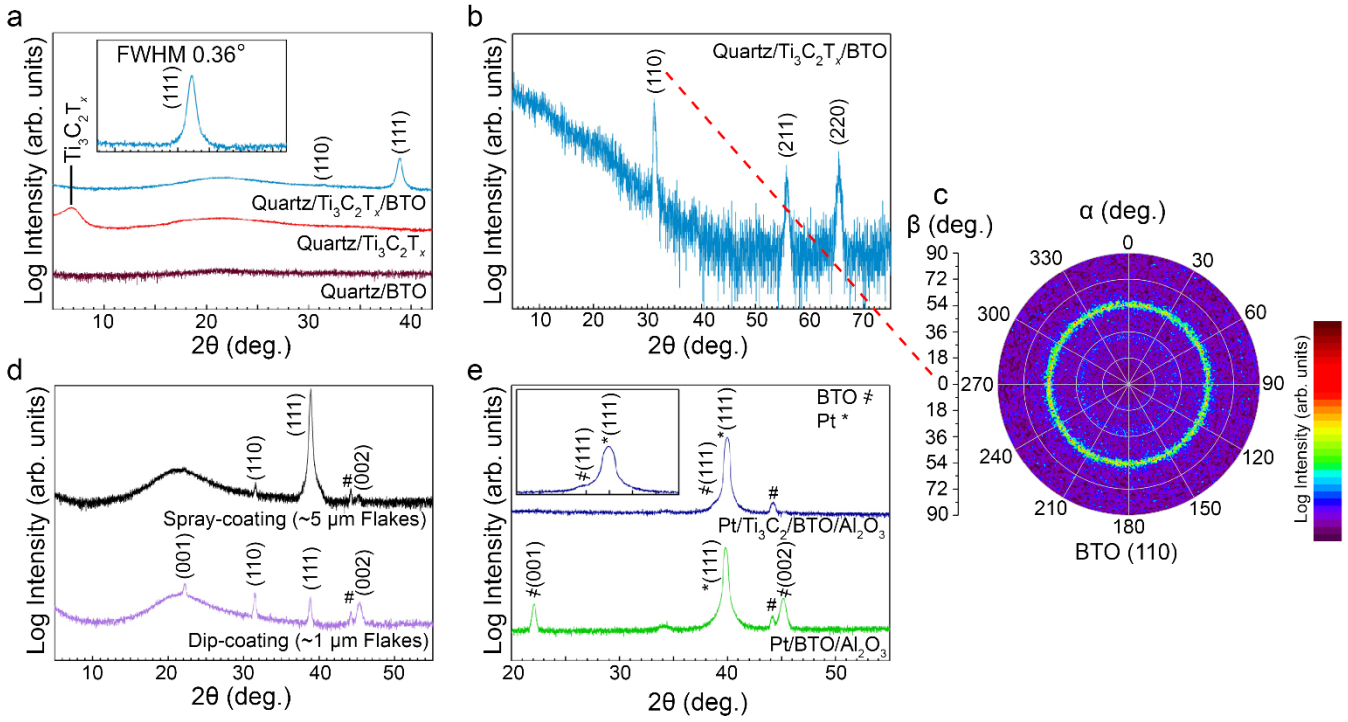

Fig. 2 (a) XRD of BTO films (≈100 nm) grown on quartz with and without MXene layer (64 nm). The inset of (a) shows the rocking curve of the BTO (111) peak on quartz with spray-coated MXene. (b) In-plane grazing incident scan of BTO on quartz with spray-coated MXene (64 nm). (c) In-plane pole figure on the sample in (b) around the BTO (110) reflection. (d) XRD of BTO films grown on quartz with spray-coating and dip-coating methods. (e) XRD of films grown on Pt with and without MXene layer. The inset of (e) shows the region around the BTO (111) and the Pt (111) peaks. The # denotes a peak from the sample stage.

become apparent: i) the presence of the MXene layer initiates the crystallization of BTO on an amorphous substrate at a growth temperature of 700°C, which otherwise results in an amorphous film as evident from the lack of any diffraction peaks for BTO grown directly on quartz, and ii) the addition of the MXene layer promotes highly-oriented growth along the (111) direction, despite the degradation of the MXene during the BTO deposition (Fig. 2(a)). This observation is in contrast to a similar study for graphene/STO, where the hexagonal graphene layer promotes (001)-orientation.[30] The inset of Fig. 2(a) shows the rocking curve of the (111) BTO peak, which reveals the oriented growth along this direction. The corresponding grazing incidence in-plane XRD scan (Fig. 2(b)) has diffraction maxima exclusively belonging to planes, which are orthogonal to the (111) planes, confirming the BTO film's high degree of orientation. At the same time, the occurrence of various peaks that fulfil the condition of orthogonality implies a polycrystalline nature within the plane of the BTO-film. Due to the lack of any peak splitting, we assumed a cubic symmetry in all cases and the calculated lattice parameters (Supporting Information) are summarized in Table 1.

Table 1. Calculated cubic *a*-lattice parameters of the grown BTO films on different substrates, and the XRD measurement

Sample	Measurement	*a*-lattice constant (Å)
Quartz / MXene/ BTO	Grazing Incidence	4.03 ± 0.01
	Out-of-plane	4.01 ± 0.01
Pt / BTO	Out-of-plane	4.01 ± 0.01
Pt / MXene / BTO	Out-of-plane	4.01 ± 0.01

The slight disagreement between the in-plane and out-of-plane *a*-lattice constant is most likely caused by the difference in the experimental setup; however, the difference might indicate a slightly strained growth initiated by the templating effect of $Ti_3C_2T_x$. Comparing the *a*-lattice constant of the BTO film to literature shows that the *a*-lattice constants of our films compare very well with unstrained films.[36] An in-plane pole figure[37] (Fig. 2(c)), collected for the sample from Fig. 2(b), around the BTO (110) peak shows that the film is textured. The ring shape from the pole figure indicates that the (110) planes of BTO lack a preferred in-plane orientation, which is a result of the BTO film templating from the random in-plane orientation of the MXene flakes.

Interestingly, the initial lateral size of the $Ti_3C_2T_x$ flakes used for the MXene layer also determines the degree of preferred (111) orientation of the BTO film (Fig. 2(d)). This is evidenced by the use of smaller lateral sized MXene flakes for the dip-coating method, which significantly reduces the preferred growth orientation along the (111) direction and the deposited BTO film has a more random grain distribution. To quantify the preference of the BTO films to grow along the (111) orientation, the ratio (I_{111}/I_{110}) of the integral intensities of the (111) to (110) peaks were determined for both, the spray- and dip-coated MXene/BTO samples. For the spray-coated sample, I_{111}/I_{110} is above 31,000 compared to randomly oriented powder, which has an intensity ratio of 0.24.[38] For the dip coated sample with a layer of smaller MXene flakes, the I_{111}/I_{110} drops to about 1, which implies a strongly reduced preference for the (111) orientation. In turn, this observation suggests a level of control for the fraction of (111) oriented BTO grains in the films over other crystallographic directions by controlling the size of the

MXene flakes. In both cases our deposition conditions produce (111) and (110) oriented films, which differ significantly from randomly oriented powder. Finally, it is also important to note that for both, the spray- and dip-coated MXene/BTO samples, the BTO deposition causes the complete decomposition of $Ti_3C_2T_x$, which is evident from the lack of the (002) MXene peak. The strong preference of the BTO film to grow along the (111) direction can be attributed to a similar atomic structure between the out-of-plane surface of the $Ti_3C_2T_x$ MXene flakes, which has a hexagonal crystal structure,[34] and the perovskite crystal structure along the (111) direction which has a buckled honeycomb lattice.[39]

Another set of samples was fabricated on Pt-silicon using larger laterally sized (5 µm) MXene flakes applied through the spray-coating method to probe the influence of the $Ti_3C_2T_x$ seed layer on the resulting properties. For this purpose, a reference BTO sample was grown directly on Pt-silicon without the MXene layer (Fig. 1(b) and (c)). In both cases, an amorphous capping layer of 3 nm thick Al_2O_3 was deposited by ALD after the PLD-growth of BTO to inhibit leakage current through pinholes in the films, due to the large size difference between the platinum top electrodes (90 x 90 µm) and the BTO film that templates off the MXene flakes (≈ 5 µm in diameter). As such there are many grain boundaries (Fig. 3) that can provide conductive pathways which reduces electrical performance.

The XRD patterns of these films are depicted in Fig. 2(e). While the BTO film directly grown on Pt-silicon only shows (00*l*) peaks (Fig. 2(e)), it has been reported in literature that the resultant film orientation from the non-equilibrium PLD growth process is strongly dependent on the deposition conditions. Silva *et al.* explored the effect of the laser repetition rate on the XRD pattern.[40] They showed that for a higher repetition rate, the (100) BTO peak is suppressed and the (110) and the (111) peaks are enhanced. Additionally, Cheng *et al.* reported on the influence of the substrate temperature on the BTO films.[41] While in their work, the (001) and the (111) peaks of BTO are present at all temperatures in the XRD patterns, the (110) peak is affected by the substrate temperature with the (110) peak intensity declining as the substrate temperature decreases until it vanishes at a temperature of 450°C. As in the present study the deposition conditions remained unchanged, comparison of the two films grown on Pt-silicon implies that the MXene layer is able to completely change the preferred orientation of resulting films from the (001) to the (111) direction, similar to what was observed on the quartz substrate. From the calculated lattice parameter, both films have an *a*-lattice constant of 4.01 Å, which is close to the bulk value from powder diffraction[38] indicating that the deposited BTO films have no in-plane strain imparted by the substrate. From these results, it is clear that the MXene flakes induce a preferred growth in the (111) direction of the BTO film independent from the underlying substrate, despite the decomposition of the MXene film. We hypothesize that this templating effect is very similar to the growth of, *e.g.*, (001) oriented STO on (001) oriented Si, where the initial growth of the oxide on Si defines the orientation and a subsequent formation of SiO_x at the Si/STO interface during the continuous growth of STO under oxidizing conditions causes no interruption in the growth orientation.[42] Therefore, we conclude that the stability of the MXene flakes is a decisive factor for initiating the growth of the BTO film in the (111) direction. This hypothesis is supported by the aforementioned results for differently sized MXene flakes, which alter the growth direction of the oxide film with a reduced (111) preference for smaller sizes. Interestingly, independent of the flake size, the crystallization of BTO is strongly promoted as opposed to the deposition directly on quartz resulting in an amorphous film.

Scanning Probe Microscopy and Piezoelectric Force Microscopy

Scanning probe microscopy (SPM) images were collected on the BTO films grown on the quartz substrates and are depicted in Fig. 3. Interestingly, the resulting surfaces of the BTO films grown on the 12 nm thick MXene layers show that the BTO films have adopted a similar surface morphology as the MXene flakes. The morphology results from our samples are similar to those reported by Wang *et al.* for hafnium oxide on MXene-glass substrates. Unlike the HfO_2 films, which were deposited by ALD at 160°C using water as the oxygen source[43] to minimize any potential degradation of the MXene, the BTO films were deposited at a temperature of 700°C under partial oxygen pressure. As mentioned above, high temperature in the presence of oxygen significantly degrades the $Ti_3C_2T_x$ MXene flakes, ultimately causing complete decomposition. While the MXene layer in our samples is certainly decomposed after the deposition (Fig. 5), the BTO film not only adopts a preferred orientation, but also preserves the shape of the flakes for its own grains. From the SPM images (Fig. 3), it becomes clear that the in-plane grain size of the BTO film is governed by the initial size of the MXene flakes. This observation provides further evidence for the suggested templating effect occurring during the initial growth of BTO before the decomposition of $Ti_3C_2T_x$.

Piezoresponse force microscopy (PFM) scans and switching spectroscopy PFM (SS-PFM) were conducted on a BTO film that was grown on a MXene spray-coated Pt-silicon and lacked the Al_2O_3 capping layer. The initial PFM scan shows a distinct difference in the amplitude and phase plots compared with the topology of the film (compare Figs. 4(a), (b), and (c)) demonstrating that the deposited BTO film has a piezoelectric response with domains of ≈180° phase difference over the 5 µm

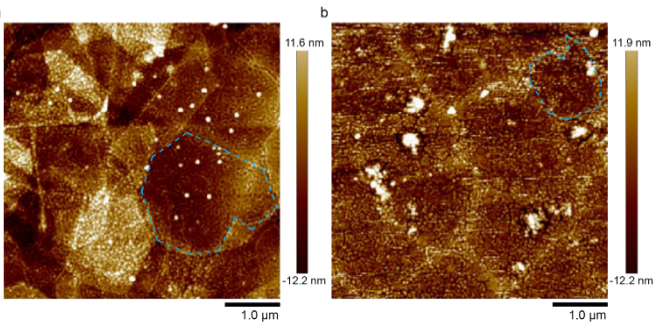

Fig. 3 SPM images showing the surface morphology of the BTO films grown on quartz substrates with 12 nm thick MXene layers, (a) spray-coating method with an average flake size of 5 µm, and (b) dip-coating method with an average flake size of 1 µm. the dashed blue outlines highlight representative BTO grains. Note: these two films have a 12 nm thick layer of $SrRuO_3$ deposited between the substrate and the BTO film.

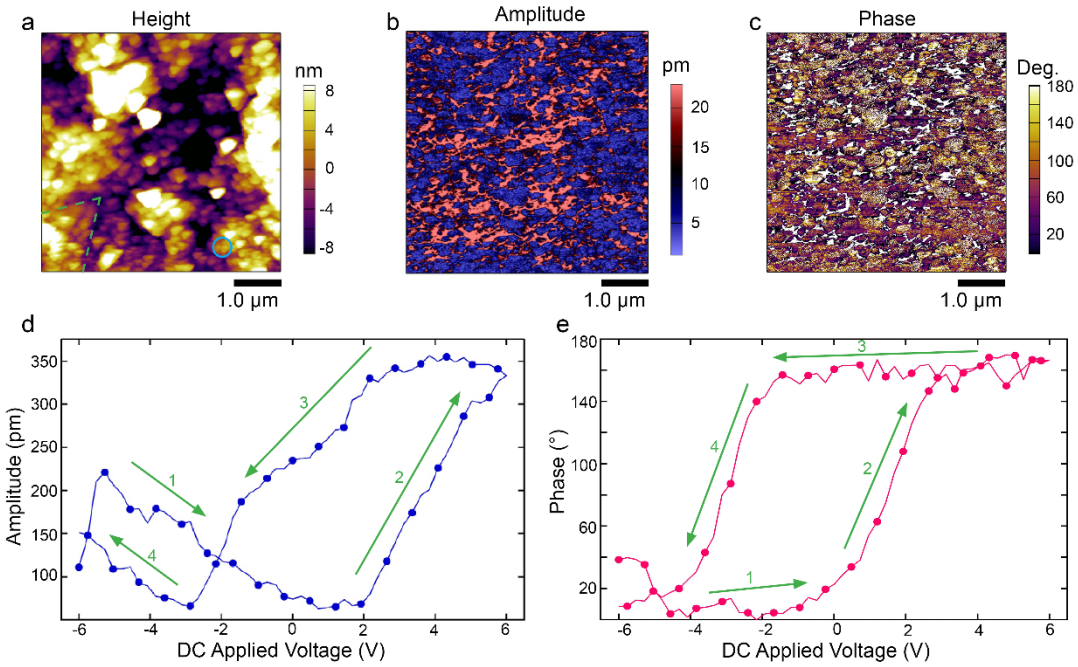

Fig. 4 PFM images and SS-PFM loops of a Pt-Silicon/$Ti_3C_2T_x$/BTO sample. (a) Topography of a 5 µm x 5 µm scan area, the dashed green line indicates the outline of the morphology of a BTO grain and the light blue circle indicates the point, where the point-wise SS-PFM was conducted. (b) amplitude, and (c) phase. The amplitude (d), and phase (e) response of the SS-PFM. The phase difference is ≈170°.

x 5 µm area. Point-wise SS-PFM was conducted to determine the ferroelectric behavior of the BTO film and is provided for a representative location marked by the light blue circle in Fig. 4(a). The amplitude and phase results (Fig. 4(d), (e)) show a signature ferroelectric response consistent with that found in other ferroelectric oxide films,[44] confirming that despite the decomposition of the MXene under the deposition conditions, deposited BTO films are ferroelectric.

Transmission Electron Microscopy

A transmission electron microscopy (TEM) cross-section of the MIM-capacitor structure (Pt-MXene-BTO-Al_2O_3-Pt) was investigated to examine the morphology of the BTO film and the interfaces with the electrodes. In Fig. 5(a), the Pt-electrodes are separated by ≈100 nm of BTO. In addition, a thin bright layer on top of the BTO film indicates the presence of the ALD-grown Al_2O_3. In general, the morphology of the BTO film exhibits predominantly columnar grains extended perpendicular to the substrate surface corroborating the XRD results. The rough surface of the Pt bottom electrode results from the Piranha acid treatment (Supporting Information) prior to the MXene deposition. A closer inspection of the interface between the bottom electrode and the BTO film reveals that the atomic planes of BTO extend to the interface without any indication of the presence of MXene or any amorphous or Ti-rich phase (see Fig. 5(b)). This lack of impurities implies that the excess Ti is dissolved in the BTO film, while the carbon of the $Ti_3C_2T_x$ layer outgases during the decomposition as CO_y at 700°C. In Fig. 5(c) the interface with the top electrode is shown. The ≈3 nm thick ALD grown Al_2O_3 film is clearly amorphous, while a well-crystallized BTO film is present below.

An energy dispersive spectroscopy (EDS)-line scan as presented in Fig. 6 on a scanning–TEM (STEM) image indicates a minor change in composition of the BTO film from the bottom to the top electrode. While the Ti-content by trend decreases in the BTO film from the bottom to the top electrode, there is a slight increase of Ba. This change is consistent with a surplus of Ti from the decomposed 12 nm thick $Ti_3C_2T_x$ layer. Interestingly, the oxygen content decreases towards the top electrode, which could be related to the PLD-growth conditions, but could also

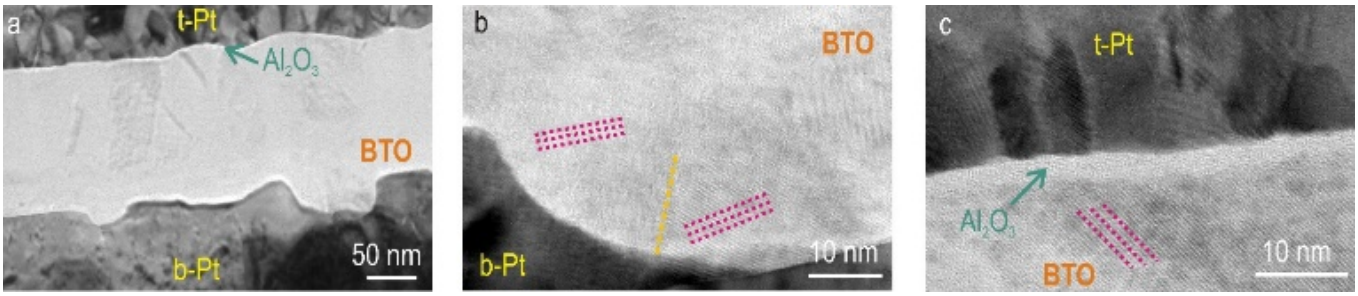

Fig. 5 (a) TEM image of the MIM-capacitor cross section outlined in Figure 1b, (b) interface between the bottom Pt-electrode (b-Pt) and the BTO film, BTO grains with different orientations are highlighted (c) interface between the top Pt-electrode (t-Pt), the Al_2O_3 layer and the BTO film with atomic plane orientations highlighted by pink dashed lines.

be an artifact from the vicinity to the 3 nm thick Al_2O_3 layer, which was not resolved during the EDS-line scan.

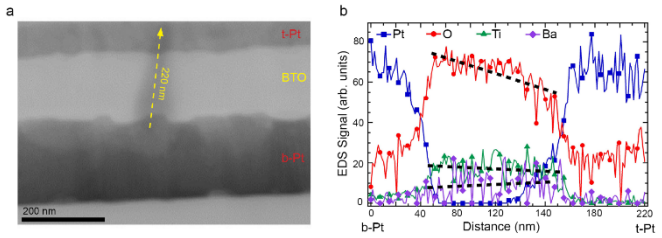

Fig. 6. (a) STEM image of the MIM-capacitor cross section outlined in Figure 1b, with the line scan for EDS highlighted by the yellow dashed line. The arrow indicates the scan direction. (b) EDS-signal as a function of position along the dashed line indicated in Figure 6a.

Electrical Characterization

The electrical properties in reference to a BTO film without MXene grown under identical PLD-conditions, were measured for the two MIM-structures outlined in Fig. 1(b) and (c) and are displayed in Fig. 7. The thin ≈3 nm thick layer of Al_2O_3 was deposited to prevent leakage from pinholes and/or conduction paths in the films. The frequency dependence of the dielectric constant and the losses (Fig. 7(a)) reveal that there is little to no frequency dependence of the dielectric constant or the loss tangent in the measured range of 10 kHz to 1 MHz for both MIM structures. The very similar magnitude as well as frequency dependence of permittivity and dielectric losses in both films demonstrate that the dielectric properties do not deteriorate when a MXene seed layer is used. The electric field dependences of the dielectric constant and losses displayed in Fig. 7(b) show in both cases a small asymmetry. The larger dielectric constant ($\varepsilon_r \approx 123$) for the (001)-oriented film can be explained by the orientation of the TiO_6 octahedra with the applied field. In comparison, Appleby *et al.* showed for Pt/BTO/Pt heterostructures with polycrystalline BTO layers containing columnar grains that the room temperature dielectric constant decreased rapidly for film thicknesses of 380 to 160 nm, where the thinnest film studied (160 nm thickness) had a dielectric constant of ≈325.[45] This observation is in line with finite size scaling effects for films with columnar grain morphology.[46] Taking these effects into account, the dielectric constant of (ε_r ≈102) extracted for the (111)-oriented BTO film is well within the expected range for 100 nm film thickness. While the plot of the dielectric response to applied field does not show a typical response of a ferroelectric material,[47] SS-PFM on a single BTO grain template from a single MXene flake shows a ferroelectric response both in the phase and amplitude measurements (Fig. 4d, e) which has the same distinct features in the work by others.[48–50]

Overall, our results demonstrate that the properties of the BTO layer are only marginally affected, when utilizing a MXene layer as degradable crystallization template. We expect that improvements in the deposition process such as adjustments to the PLD-growth (*e.g.*, Ti-deficient target for the initial growth) and the uniformity of the MXene layer (flake size, roughness) may enable improved ferroelectric and dielectric performance. A significant challenge is to increase the size of the MXene flakes which is determined by the grain size of the starting MAX Phase (M = early transition metal, A = group 13-16 elements, and X = C or N)[51] and etching and delaminating conditions. We have reported MXene flakes as larger as 10 µm which was used in field-effect transistor device,[52] however these flakes were not used in this work.

Conclusions

In summary, $BaTiO_3$ thin films were grown by PLD on quartz glass and Pt-silicon substrates with seed layers of $Ti_3C_2T_x$ MXene flakes acting as degradable template to promote highly oriented growth. Our results show that the high temperature and oxygen rich environment used in the BTO growth cause the MXene layer to fully degrade, but the resultant BTO film has a preferred growth orientation along the (111) direction. This templating effect is independent of the substrate and strongly promotes crystallization on amorphous underlayers. During the growth process, the BTO film is able to adopt and preserve the morphology of the initial MXene flakes throughout the deposition. The BTO films possess a cubic lattice parameter that

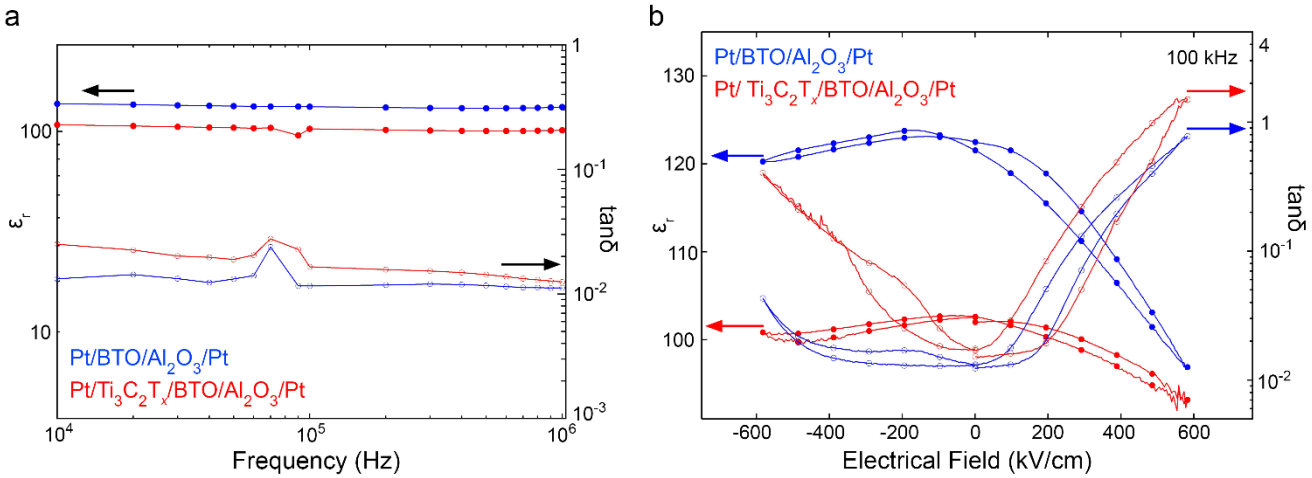

Fig. 7 (a) Dielectric constant, ε_r, and loss tangent, *tan δ*, as a function of frequency at zero applied field, and (b) Plot of dielectric constant and loss as a function of applied electric field collected at 100 kHz. Note: spray-coated MXene was applied for the films used in the electrical characterization.

is consistent with the bulk value, suggesting that BTO films can be grown on different substrates without inducing large strains into the film using this method, which would typically cause dislocation and defect formation. In addition to the highly oriented film, the selection of the MXene lateral flake size provides a degree of control over the fraction of the film that grows in a specific direction, where larger MXene flakes promote growth along the (111) direction. TEM images show columnar grains, and the absence of the initial MXene layer and any other impurities at the bottom interface confirms that the MXene decomposes during the deposition, where surplus Ti is accommodated in the BTO film and the carbon outgases as CO_y. PFM and SS-PFM show that the BTO film grown with the MXene layer retains its ferroelectric behavior and has a robust piezoelectric response. Electrical measurements reveal that the BTO film on MXene coated Pt-silicon has a comparable dielectric constant and loss tangent to a BTO film grown on bare Pt-silicon substrate. Our results demonstrate that $Ti_3C_2T_x$ flakes provide a temporary seed layer that promotes crystallization of unstrained BTO thin films without hindering the electrical or ferroelectric properties. As both, the spray-and dip-coating methods for MXene depositions can be cost-effectively completed on virtually any sized substrate, this approach provides a powerful tool for the growth of highly oriented BTO films on a wide variety of substrates.

Conflicts of interest

There are no conflicts to declare.

Acknowledgements

A.B.-J. was supported by a Hearst Foundation Doctoral Fellowship. Y.G., K.H. and B.A. were supported by the U.S. Department of Energy (DOE), Office of Science, Office of Basic Energy Sciences, grant #DE-SC0018618. M.F., A.P. and J.E.S. acknowledge support from the Office of Naval Research under grant no. N00014-15-11-2170, Z.G. acknowledges support from the Army Research Office under grant no. W911NF-14-1-0500, D.I. acknowledges support from the Air Force Office of Scientific Research under grant no. FA9550-13-1-0124, and A.W.-C. acknowledges support from the NSF under DMR 1608887. This work was carried out in part at the Singh Center for Nanotechnology, which is supported by the NSF National Nanotechnology Coordinated Infrastructure Program under grant NNCI-1542153.

References

1 J. P. Attfield, *Crystal Engineering*, 2002, **5**, 427-438.
2 Z. Gu, S. Pandya, A. Samanta, S. Liu, G. Xiao, C. J. G. Meyers, A. Damodaran, H. Barak, A. Dasgupta, S. Saremi, A. Polemi, L. Wu, A. Podpirka, A. Will-Cole, C. J. Hawley, P. K. Davies, R. A. York, I. Grinberg, L. W. Martin, and J. E. Spanier, *Nature*, ***560*** 2018, 622-627.
3 Z. Gu, D. Imbrenda, A. L. Bennett-Jackson, M. Falmbigl, A. Podpirka, T. C. Parker, D. Shreiber, M. P. Ivill, V. M. Fridkin and J. E. Spanier, *Phys. Rev. Lett.*, 2017, **118**, 1–5.
4 J. E. Spanier, V. M. Fridkin, A. M. Rappe, A. R. Akbashev, A. Polemi, Y. Qi, Z. Gu, S. M. Young, C. J. Hawley, D. Imbrenda, G. Xiao, A. L. Bennett-Jackson and C. L. Johnson, *Nat. Photonics*, 2016, **10**, 611–616.
5 S. Pandya, J. Wilbur, J. Kim, R. Gao, A. Dasgupta, C. Dames and L. W. Martin, *Nat. Mater.*, 2018, **17**, 432–438.
6 X. D. Wu, S. R. Foltyn, R. C. Dye, Y. Coulter and R. E. Muenchausen, *Appl. Phys. Lett.*, 1993, **62**, 2434–2436.
7 J. Wang, J. B. Neaton, H. Zheng, V. Nagarajan, S. B. Ogale, B. Liu, D. Viehland, V. Vaithyanathan, D. G. Schlom, U. V Waghmare, N. A. Spaldin, K. M. Rabe, M. Wuttig and R. Ramesh, *Science*, 2003, **299**, 1719–1722.
8 Y. Tokunaga, N. Furukawa, H. Sakai, Y. Taguchi, T. H. Arima and Y. Tokura, *Nat. Mater.*, 2009, **8**, 558–562.
9 R. Ramesh, D. Hwang, T. S. Ravi, A. Inam, J. B. Barner, L. Nazar, S. W. Chan, C. Y. Chen, B. Dutta, T. Venkatesan and X. D. Wu, *Appl. Phys. Lett.*, 1990, **56**, 2243–2245.
10 D. V. Taylor and D. Damjanovic, *J. Appl. Phys.*, 1997, **82**, 1973–1975.
11 J. Seidel, L. W. Martin, Q. He, Q. Zhan, Y. H. Chu, A. Rother, M. E. Hawkridge, P. Maksymovych, P. Yu, M. Gajek, N. Balke, S. V. Kalinin, S. Gemming, F. Wang, G. Catalan, J. F. Scott, N. A. Spaldin, J. Orenstein and R. Ramesh, *Nat. Mater.*, 2009, **8**, 229–234.
12 J. Seidel, D. Fu, S. Y. Yang, E. Alarcón-Lladó, J. Wu, R. Ramesh and J. W. Ager, *Phys. Rev. Lett.*, 2011, **107**, 1–4.
13 H. N. Lee, S. M. Nakhmanson, M. F. Chisholm, H. M. Christen, K. M. Rabe and D. Vanderbilt, *Phys. Rev. Lett.*, 2007, **98**, 98–101.
14 D. Pesquera, G. Herranz, A. Barla, E. Pellegrin, F. Bondino, E. Magnano, F. Sánchez and J. Fontcuberta, *Nat. Commun.*, 2012, **3**, 1–7.
15 A. Vailionis, H. Boschker, W. Siemons, E. P. Houwman, D. H. A. Blank, G. Rijnders and G. Koster, *Phys. Rev. B - Condens. Matter Mater. Phys.*, 2011, **83**, 1–10.
16 R. Xu, S. Liu, I. Grinberg, J. Karthik, A. R. Damodaran, A. M. Rappe and L. W. Martin, *Nat. Mater.*, 2015, **14**, 79–86.
17 A. T. Zayak, X. Huang, J. B. Neaton and K. M. Rabe, *Phys. Rev. B*, 2006, **74**, 94104.
18 R. A. McKee, F. J. Walker and M. F. Chisholm, *Phys. Rev. Lett.*, 1998, **81**, 3014–3017.
19 L. Zhang and R. Engel-Herbert, *Phys. Status Solidi RRL*, 2014, **8**, 917–923.
20 L. Mazet, S. M. Yang, S. V Kalinin, S. Schamm-Chardon and C. Dubourdieu, *Sci. Technol. Adv. Mater.*, 2015, **16**, 36005.
21 C. Xiong, W. H. P. Pernice, J. H. Ngai, J. W. Reiner, D. Kumah, F. J. Walker, C. H. Ahn and H. X. Tang, *Nano Lett.*, 2014, **14**, 1419–1425.
22 Y. J. Hong, W. H. Lee, Y. Wu, R. S. Ruoff and T. Fukui, *Nano Lett.*, 2012, **12**, 10–15.
23 Y. Shi, W. Zhou, A.-Y. Lu, W. Fang, Y.-H. Lee, A. L. Hsu, S. M. Kim, K. K. Kim, H. Y. Yang, L.-J. Li, J.-C. Idrobo and J. Kong, *Nano Lett.*, 2012, **12**, 2784–2791.
24 A. Koma, *Thin Solid Films*, 1992, **216**, 72–76.
25 Y. Alaskar, S. Arafin, D. Wickramaratne, M. A. Zurbuchen, L. He, J. McKay, Q. Lin, M. S. Goorsky, R. K. Lake and K. L. Wang, *Adv. Funct. Mater.*, 2014, **24**, 6629–6638.
26 C. Jung, T. Ohnishi, M. Osada, K. Takada and T. Sasaki, 2013, 4592–4596.
27 J. Kimura, I. Takuwa, M. Matsushima, T. Shimizu, H. Uchida, T. Kiguchi, T. Shiraishi, T. J. Konno, T. Shibata, M. Osada, T. Sasaki and H. Funakubo, *Sci. Rep.*, 2016, **6**, 1–9.
28 T. Shibata, Y. Ebina, T. Ohnishi, K. Takada, T. Kogure and T. Sasaki, *Cryst. Growth Des.*, 2010, **10**, 3787–3793.
29 T. Shibata, H. Takano, Y. Ebina, D. S. Kim, T. C. Ozawa, K. Akatsuka, T. Ohnishi, K. Takada, T. Kogure and T. Sasaki, *J. Mater. Chem. C*, 2014, **2**, 441–449.

30 S. A. Lee, J. Y. Hwang, E. S. Km, S. W. Kim and W. S. Choi, *ACS Appl. Mater. Interfaces*, 2017, **9**, 3246–3250.
31 T. Shibata, K. Fukuda, Y. Ebina, T. Kogure and T. Sasaki, *Adv. Mater.*, 2008, **20**, 231–235.
32 O. Mashtalir, M. Naguib, V. N. Mochalin, Y. Dall'Agnese, M. Heon, M. W. Barsoum and Y. Gogotsi, *Nat. Commun.*, 2013, **4**, 1–7.
33 M. Acosta, N. Novak, V. Rojas, S. Patel, R. Vaish, J. Koruza, G. A. Rossetti and J. Rödel, *Appl. Phys. Rev.*, 2017, **4**, 041305.
34 B. Anasori, M. R. Lukatskaya and Y. Gogotsi, *Nat. Rev. Mater.*, 2017, **2**, 16098.
35 K. Hantanasirisakul, M.-Q. Zhao, P. Urbankowski, J. Halim, B. Anasori, S. Kota, C. E. Ren, M. W. Barsoum and Y. Gogotsi, *Adv. Electron. Mater.*, 2016, **2**, 1600050.
36 J. J. Wang, F. Y. Meng, X. Q. Ma, M. X. Xu and L. Q. Chen, *J. Appl. Phys.*, 2010, **108**, 034107.
37 S. Kobayashi, *Rigaku J.*, 2010, **26**, 3–11.
38 P. Villars and K. Cenzual, Pearson's Crystal Data: Crystal Structure Database for Inorganic Compounds (on DVD), ASM International®, Materials Park, Ohio, USA.
39 G.A. Fiete and A. Rüegg, J. *Appl. Phys.*, 2015, **117**, 172602.
40 J. P. B. Silva, K. C. Sekhar, a. Almeida, J. A. Moreira, M. Pereira and M. J. M. Gomes, *Appl. Phys. A Mater. Sci. Process.*, 2013, **113**, 379–384.
41 C. Hsiu-Fung, Y. Ming-Hua, L. Kuo-Shung and L. I-Nan, *Jpn. J. Appl. Phys.*, 1993, **32**, 5656–5660.
42 Z. Yu, J. Ramdani, J. A. Curless, C. D. Overgaard, J. M. Finder, R. Droopad, K. W. Eisenbeiser, J. A. Hallmark, W. J. Ooms and V. S. Kaushik, *J. Vac. Sci. Technol. B Microelectron. Nanom. Struct.*, 2000, **18**, 2139.
43 Z. Wang, H. Kim and H. N. Alshareef, *Adv. Mater.*, 2018, **1706656**, 1–7.
44 H. Pang, F. Zhang, M. Zeng, X. Gao, M. Qin, X. Lu, J. Gao, J. Dai and Q. Li, *npj Quantum Mater.*, 2016, **1**, 16015.
45 D. J. R. Appleby, N. K. Ponon, K. S. K. Kwa, S. Ganti, U. Hannemann, P. K. Petrov, N. M. Alford and A. O'Neill, *J. Appl. Phys.*, 2014, **116**, 124105.
46 J. F. Ihlefeld, D. T. Harris, R. Keech, J. L. Jones, J. P. Maria and S. Trolier-McKinstry, *J. Am. Ceram. Soc.*, 2016, **99**, 2537–2557.
47 B.H. Hoerman, G.M. Ford, L.D. Kaufmann, and B.W. Wessels, *Appl. Phys. Lett.*, 1998, **73**, 2248.
48 P. Ponath, K. Fredrickson, A.B. Posadas, Y. Ren, X. Wu, R.K. Vasudevan, M. Baris Okatan, S. Jesse, T. Aoki, M.R. McCartney, D.J. Smith, S. V. Kalinin, K. Lai, and A.A. Demkov, *Nat. Commun.*, 2015, **6**, 6067.
49 K. Suzuki, T. Hosokura, T. Okamoto, J. Steffes, K. Murayama, N. Tanaka, and B.D. Huey, J. *Am. Ceram. Soc.*, 2018, **101**, 4677-4688.
50 C. Dragoi, M. Cernea, and L. Trupina, *Appl. Surf. Sci.*, 2011, **257**, 9600-9605.
51 M.W. Barsoum, *MAX Phases Properties of Machinable Ternary Carbides and Nitrides,* John Wiley & Sons, *Weinheim, 2013.*
52 A. Lipatov, M. Alhabeb, M.R. Lukatskaya, A. Boson, Y. Gogotsi, and A. Sinitskii, *Adv. Electron. Mater., 2016,* **2**, 1600255.

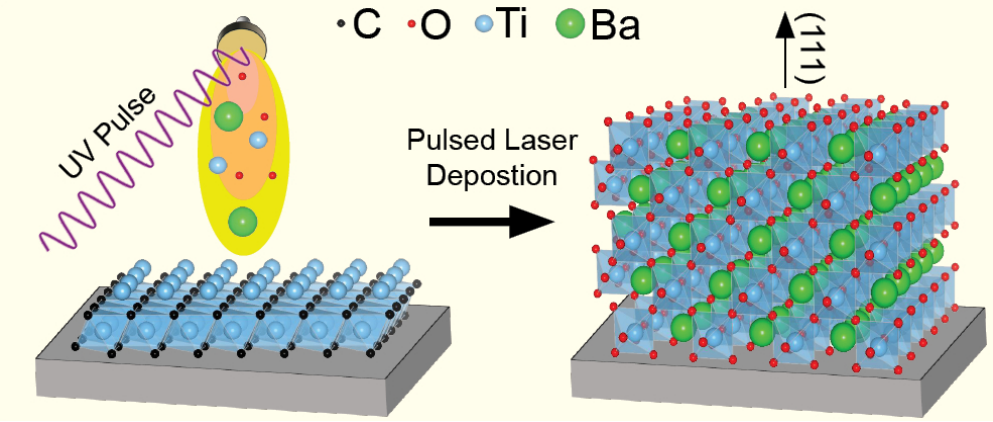

349x148mm (72 x 72 DPI)